

Finding the exact solution using an inexact model; A recursive approach for inverse modelling

Eyal Baruch^{1,a} and Izhak Bucher^{1,b}

1 – Dynamics Laboratory, Faculty of Mechanical Engineering, Technion – Israel Institute of Technology,
Haifa 3200003, Israel

Date: March 12, 2023

Keywords: successive approximation, topography reconstruction, system identification, atomic force microscopy, autoresonance, inverse modelling

^a Electronic mail: eyalbaruch@campus.technion.ac.il

^b Electronic mail: bucher@technion.ac.il

Abstract

Nonlinear systems and interaction forces can be challenging to accurately identify due to their complex behaviour. This problem intensifies for continuous systems undergoing distributed, coupled interactions, such as in the case of topography measurement systems. Presented is a method to invert a set of nonlinear coupled equations, which can be functions of unknown distributed physical quantities. The method employs an invertible approximate model-based successive approach to iteratively converge to the exact solution of the set of nonlinear equations, while a non-invertible exact model is used to estimate the error. This is done by exploiting a simplified physical model, alleviating some of the sensitivity and singularity issues related to inverse problems.

As a case study, we demonstrate the effectiveness of our method by applying it to the problem of reconstructing the topography of surface contours using a thin and long vibrating fiber. In nanoscale metrology, measuring inaccessible deep and narrow grooves or steep walls becomes difficult and singular when attempting to extract distributed nonlinear interactions that depend on the topography. We verify our method numerically by simulating the Van der Waals (VdW) interaction forces between a nanofiber and a nanoscale topography, and experimentally by exploiting magnetic interactions between a magnetic topography and a vibrating, elastic beam. Our results show that our method can accurately reconstruct the topography of normally inaccessible regions, making it a valuable tool for a wide range of applications involving nonlinear inverse problems.

1. Introduction

A method for solving a set of coupled nonlinear equations is presented for physically inspired inverse problems. By exploiting a simplified inverse model, the method converges to the solution of the full model without explicitly inverting it. As a case study, the method is implemented on a problem of reconstructing the topography of optically inaccessible domains of micro or nanoscale devices. This is done by estimating the effect of distributed coupling forces. The projection of distributed inter-molecular forces between the specimen's surface and an oscillating nanofiber is recovered using the aforementioned approach. The latter overcomes several obstacles, including smearing, time consuming control methods, singular model inversion, and inaccurate inverse modeling.

System identification and parameter estimation are crucial and evolving areas of research [1], due to challenges regarding robustness to noise and singularity, and their imperative significance in the industrial sector for practical uses such as control and identification. A main challenge in this field is that the underlying equations can become singular when the measured data is not sufficiently informative. In addition, even when the data is theoretically sufficient, in situations where the mapping between the measurements and fitted parameters is nonlinear [2–7], numerically inverting the system can become ill-posed or impossible. As a result, nonlinear system identification (e.g. [8]) calls for a unique set of tools and is often restricted to a small number of parameters.

Many approaches have been proposed to address these challenges, ranging from direct, simple methods such as least squares [2], to complex, black-box methods such as deep neural networks. Reference [9] presented a method iteratively combining experimentation and post-processing to extract the dynamics of a given system. Reference [10] used genetic algorithms to determine the minimal set of dynamic equations that accurately reproduce measurements from a dynamic system. Reference [11] utilized a sparse set of modes to evolve the solution of partial differential equations over time, and [12] constructed a set of localized modes used to solve Schrödinger's equation for N particles. In [13] it was proposed to build a library of functions for sparse identification of the model. Additionally, [14] developed an algorithm encompassing a wide range of methods, from dimensional analysis to neural networks, to enable system identification, while [15] integrated the partial differential equations of a dynamic system into the objective loss function of a neural network approximating the response of the dynamic system. Lastly, the process of modeling and identifying the dynamics of a system using a digital twin [16] was also explored.

Despite the mentioned apparent attempts, finding the inverse of a nonlinear multi-parameter problem remains a great challenge, especially where efficiency and speed are important. Singularity can sometimes be treated via regularization [17], such is the case in Atomic Force Microscopy (AFM) [18], which is a

commonly used method for nanoscale metrology. This method utilizes Van der Waals (VdW) interactions between a sharp tip and the measured sample to reconstruct the topology of samples in atomic resolution. AFM is implemented using a variety of techniques, including Frequency Modulated AFM, which measures the change in the resonance frequencies of the system [19], due to changes in the overall potential affected by the spacing of interacting molecules in the sensor and specimen. However, AFM has several limitations. Firstly, the tip size makes it more difficult to measure complex, irregular topographies. This has been addressed partially by using different shaped tips [20–22] and tilting the AFM cantilever [23]. In spite of this, accurately measuring the contours of grooves remains a challenge. Secondly, AFM utilizes a point-by-point scan of the topography, tracking the natural frequency using phase-locked loop to find the distance of the cantilever from each point [24]. This is a time-consuming method, rendering it unusable for many applications. Thirdly, AFM works on the assumption that the tip interacts with a single point or atom per measurement [25]. It was shown that this assumption can be inaccurate, especially in groove-like topographies, resulting in significant smearing of the approximation in some cases [26].

This paper presents a comprehensive approach to overcome some of these problems. By introducing a model-based successive approximation (MBSA) method, it is made possible to implicitly invert the set of coupled equations, using a simplified invertible model. For the AFM study case, this method is utilized to decouple distributed interactions between the topography and a thin, elongated vibrating fiber, which can be inserted into complex topographies. Successive approximation can be utilized to solve coupled nonlinear equations [27] and is implemented in a variety of applications, such as ADC converters [28], demosaicing [29], and optimal control design for nonlinear systems [30]. By decoupling the distributed interactions, the AFM method can accurately approximate grooves, reducing the smearing resulting from the localized interaction assumption. In addition, introducing a model of the interactions is faster than the frequency tracking method, where the distance is measured by moving the sensing tip to a distance in which a fixed resonance frequency takes place. The process of moving the sensing tip with a control circuit takes time and induces measurement uncertainties.

To verify the proposed method, a simulation of a resonating nanofiber measuring a groove was conducted. The distributed VdW interactions are successfully decoupled to accurately approximate the topography. In addition, a scaled experimental system that utilizes magnetic forces was constructed to realize the method experimentally. Since the magnetic potential is a function of the gap between material points on the nanofiber and the specimen to a certain negative power, similarly to the VdW potential, the approximation of a magnetic topography via magnetic interactions can be analogous to the exploitation of VdW interactions in AFM and is thus considered as a reasonable verification.

Since nanofiber sensing and the prevalent FM-AFM [31] are based on perturbations of the system resonant frequency, Autoresonance (AR) was used to excite the system in resonance automatically at all configurations [32]. AR exploits a nonlinear element in the feedback loop (mathematically a signum function), and a 90 degrees phase shifting filter (normally an integrator), transiently inducing a positive feedback control loop to automatically excite a specific mode of vibration of the system in resonance [33,34]. The method does not require tuning of parameters like phase-locked loops and its convergence to the correct resonance frequency occurs immediately.

The paper is outlined as follows: Section 2 presents the MBSA method. Section 3 explores a case study of measuring the topography of a nanometric groove, modelling the interactions and implementing MBSA. Finally, Section 4 presents an experimental validation of the method using a magnetic beam and topography.

2. Model based successive approximation method

To make the detailed description of the extended case study more trackable, the proposed approach reasoning is described. It is of interest to seek a set of discrete parameters denoted as \mathbf{g} which reconstruct a distributed physical quantity (DPQ), denoted as $g(\zeta)$. The property is distributed along a spatial coordinate vector ζ . The data exploited to obtain \mathbf{g} is a set of measurements:

$$\omega_d^2(\mathbf{x}) = f(\mathbf{g}, \mathbf{x}), \quad \omega_d^2(\mathbf{x}) \in \mathbb{R}^m, \quad \mathbf{g} \in \mathbb{R}^N \quad (1)$$

where \mathbf{f} is some known nonlinear model which cannot be easily inverted and \mathbf{x} is a controllable parameter, e.g. the position of the sensor with respect to the sample. By incrementally changing \mathbf{x} , the vector ω_d^2 (the square of the measurement is used for convenience, as it describes the present case) is obtained.

Since an accurate representation of a DPQ requires a large number of parameters g_i , inverting the physical nonlinear model using a standard methods such as gradient descent, can prove impossible due to the nonlinearity, complexity, and singularity of the inverted model. An alternative approach is therefore presented.

Statement of the problem

Find \mathbf{g} that minimizes: $\|\omega_d^2 - \mathbf{f}(\mathbf{g}, \mathbf{x})\|$

Solution strategy

A simplified invertible model $\mathbf{f}_s(\mathbf{g}, \mathbf{x})$ with identical inputs \mathbf{g} , and \mathbf{x} is introduced. Since the model is inaccurate, the solution of the model with the correct \mathbf{g} will yield:

$$\omega'^2 = \mathbf{f}_s(\mathbf{g}, \mathbf{x}) \quad (2)$$

where the approximate model's outcome differs from the measured one, i.e. $\omega'^2 \neq \omega_d^2$ due to the simplification of the model. $\mathbf{f}_s(\mathbf{g}, \mathbf{x})$ can be inverted, producing an estimation of the topography, via:

$$\mathbf{g}'_k = \mathbf{f}_s^{-1}(\omega_k'^2(\mathbf{x}), \mathbf{x}) \quad (3)$$

where \mathbf{g}'_k is an approximation of the parameter vector \mathbf{g} , derived from some prediction of the vector $\omega_k'^2$. It should be noted that $\mathbf{f}_s(\mathbf{g}, \mathbf{x})$ is chosen such that it can be robustly inverted, while maintaining the convergence condition that will be presented in the following section.

Convergence

Introducing the error function:

$$\mathbf{e}_k = \omega_d^2(\mathbf{x}) - \mathbf{f}(\mathbf{g}'_k, \mathbf{x}) \triangleq \omega_d^2 - \omega_k'^2 \quad (4)$$

where \mathbf{f} is the full model, assuming \mathbf{f} is injective, \mathbf{e}_k will converge to 0 for $\mathbf{g}'_k = \mathbf{g}$. The error function is used to update the invertible model in the following manner:

$$\mathbf{f}_s(\mathbf{g}'_{k+1}, \mathbf{x}) = \omega_{k+1}'^2 = \omega_k'^2 + \beta \mathbf{e}_k \rightarrow \mathbf{g}'_{k+1} = \mathbf{f}_s^{-1}(\omega_{k+1}'^2(\mathbf{x}), \mathbf{x}) \quad (5)$$

where the algorithm is initialized using:

$$\omega_1'^2 = \omega_d^2. \quad (6)$$

Equation (5) can be rearranged as:

$$\omega_{k+1}'^2 = \omega_k'^2 + \beta \left(\omega_d^2 - \mathbf{f}(\mathbf{f}_s^{-1}(\omega_k'^2, \mathbf{x}), \mathbf{x}) \right) \quad (7)$$

This method is applied iteratively until convergence. The condition for convergence (proof is presented in Appendix A) is:

$$\left(\frac{\partial \mathbf{f}_s}{\partial \mathbf{g}^T} \right)^T \frac{\partial \mathbf{f}}{\partial \mathbf{g}^T} \succ 0 \quad (8)$$

An example of the convergence method for a simple problem highlighting the various steps to convergence and its advantage on classical gradient descent based methods is presented in Appendix B. The approximation method is presented as a flowchart in Figure 1:

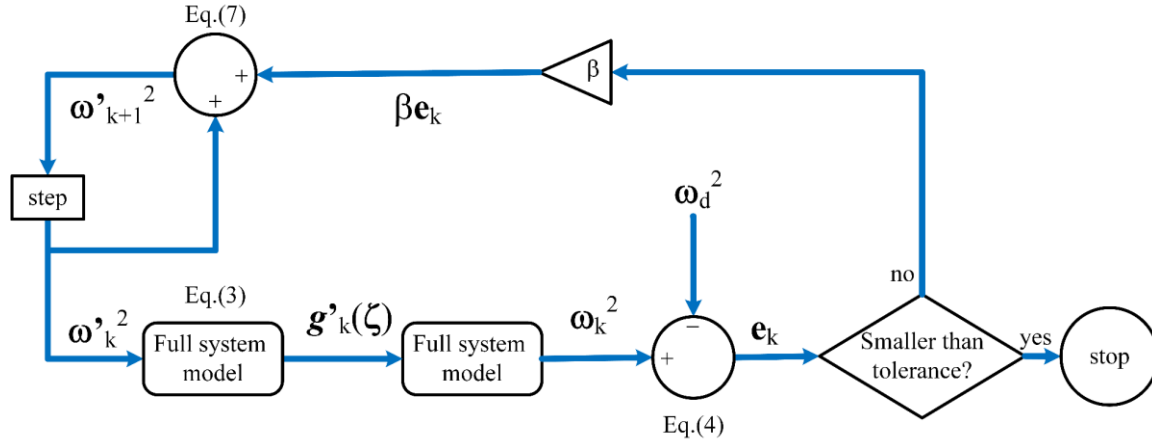


Figure 1 - A flowchart of the suggested successive approximation method

It is worth mentioning that the iterations are carried out in an offline manner and no repetitive experimentation is necessary beyond the ones generating the measurement vector, ω_d^2 . The latter introduces a great advantage over methods requiring additional experimentations [9] that are often slow and can introduce additional difficulties.

3. Case study – AFM-like nanofiber topography reconstruction

To show the power of the presented method and validate it, a model of a system incorporating the VdW interaction forces between a resonating nanofiber and a specimen was developed. A schematic of the system and the sensing nanofiber is presented in Figure 2:

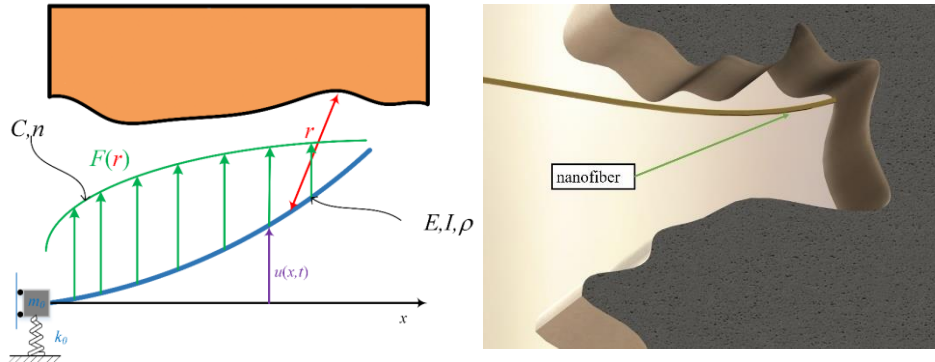


Figure 2 - The schematics of the simulated system. The oscillating fiber (in blue) interacts with the topography sample (in orange) resulting in distributed forces (in green) depending on the gap (r) between each point on the fiber and any point on the measured topography, illustrated by the red arrow. On the right, an artist's concept of the sensor and some illustrated topography is depicted.

The dynamics of this system are modeled in the following subsections.

3.1 Modeling interactions of a topography with a vibrating fiber.

Denoting C, n as the material constants describing the potential interaction for a specific configuration (see Figure 2), the interaction potential is of the form [35,36]:

$$V = \frac{C}{r^n} [kJ], \quad (9)$$

where r represents the distance between a single point on the fiber, modeled as a beam in bending, and a single point on the measured sample. The beam is parametrized as:

$$r_{beam} = (x, u_{ss}(x) + u(x, t)) \quad (10)$$

where x is a coordinate along the fiber, u_{ss} is the steady state static deflection of the beam caused by the static part of the interaction force, and u is the beam's dynamic deflection coordinate caused by an oscillating force applied to it. The surface contour of the 2D topography is parametrized as:

$$r_i = (g_1(\zeta), g_2(\zeta)), \quad (11)$$

where $\zeta \in [0, L_{top}]$ is a coordinate that follows the topography surface outline. Substituting Eq. (11) and (10) into Eq. (9) results in:

$$dV(x) = - \frac{C}{\left(\sqrt{(g_1(\zeta) - x)^2 + (g_2(\zeta) - u - u_{ss})^2} \right)^n} d\zeta. \quad (12)$$

Following [36] to replace volumetric interactions with surface interactions, the force acting on the beam will be:

$$p(x, t) = \int_0^{L_{top}} \frac{C}{(n-3)} \frac{(g_2(\zeta) - u(x, t) - u_{ss})}{\left(\sqrt{(g_1(\zeta) - x)^2 + (g_2(\zeta) - u(x, t) - u_{ss})^2} \right)^n} d\zeta. \quad (13)$$

Finally, it is assumed, without loss of generality, for sake of developing the methodology, that the bending deformations of the nanofiber can be modeled according to the Euler beam theory [37], resulting in the following partial differential (PDE) equation:

$$\rho A u_{tt} + E I u_{xxxx} = p(x, t). \quad (14)$$

where E , I , and ρ are the Young modulus, inertia, and density of the beam, and the subscripts stand for partial derivatives. The specific choice of elastic deformation model can be replaced by other models, more suitable to describe the nanofiber being used.

Eq. (14) is a highly nonlinear PDE, since $p(x)$ is a distributed force which is a function of u to some negative power. To be able to evaluate the system's response, a numerical solution employing Finite Element model including the force projected on the beam is derived. It should be emphasized that the proposed approach does not depend on the specific model of the nanofiber or the approximation method, as long as such a model can be derived.

3.2 Numerical Linearized model derivation.

Assuming the nanofiber acts according to the Euler-Bernoulli beam theory, the beam can be modeled using the appropriate Hermite beam elements, i.e. describing the deflection as a 3rd-order polynomial, as shown in [38]. The displacement of a beam element can be approximated as:

$$u_i(x_i) = \Psi_i \mathbf{a}_i, \quad \Psi_i = \begin{bmatrix} x_i^0 & x_i^1 & x_i^2 & x_i^3 \end{bmatrix} \quad (15)$$

where i represents the i_{th} beam element and N is the total number of elements. Using the transformation matrix:

$$\mathbf{R} = \begin{bmatrix} 1 & 0 & 0 & 0 \\ 0 & 1 & 0 & 0 \\ 1 & L_{elm} & L_{elm}^2 & L_{elm}^3 \\ 0 & 1 & 2L_{elm} & 3L_{elm}^2 \end{bmatrix} \quad (16)$$

the displacement of the i^{th} element q_i , and its angle θ_i can be derived, using:

$$\mathbf{q}_i = \mathbf{R} \mathbf{a}_i, \quad \mathbf{q}_i = \begin{bmatrix} q_i & \theta_i & q_{i+1} & \theta_{i+1} \end{bmatrix}^T. \quad (17)$$

Substituting Eq (17) into Eq. (15):

$$u_i(x_i) = \Psi_i \mathbf{R}^{-1} \mathbf{q}_i \quad (18)$$

The mass and stiffness matrices are then derived using:

$$M_{r,s} = \frac{\partial^2 \frac{1}{2} \rho A \int_0^L \dot{u}(x)^2 dx}{\partial \dot{q}_r \partial \dot{q}_s}, \quad K_{r,s} = \frac{\partial^2 \left(\frac{1}{2} EI \int_0^L u''(x)^2 dx \right)}{\partial q_r \partial q_s} \quad (19)$$

Using virtual work methodology [39], the projection of the force $p(x, t)$ on \mathbf{q} is:

$$F_i = \left(\int_0^{L_{elm}} (\Psi_i p(x, t)) dx \mathbf{R}^{-1} \right)^T \quad (20)$$

By discretizing $p(x, t)$ to be

$$\mathbf{p} = [p(0) \quad p(L_{elm}) \quad p(2L_{elm}) \quad \cdots \quad p(NL_{elm})] T(t), \quad (21)$$

where $T(t)$ is the time component of $p(x, t)$, Eq. (20) becomes:

$$F_i(x) = \left(\int_0^{L_{elm}} (\Psi_i (p_i(L_{elm} - x) + p_{i+1}x)) dx \mathbf{R}^{-1} \right)^T. \quad (22)$$

Rearranging:

$$F_i = \left[\left(\int_0^{L_{elm}} (\Psi_i (L_{elm} - x)) dx \mathbf{R}^{-1} \right)^T \quad \left(\int_0^{L_{elm}} (\Psi_i x) dx \mathbf{R}^{-1} \right)^T \right] \begin{bmatrix} p_i \\ p_{i+1} \end{bmatrix} = \mathbf{Q}_i \begin{bmatrix} p_i \\ p_{i+1} \end{bmatrix} \quad (23)$$

In this manner, the full projection matrix \mathbf{Q} can be constructed. The equation of motion of the beam with VdW interacting forces will be:

$$M\ddot{q} + C_d\dot{q} + Kq = \mathbf{Q}\mathbf{p}T(t), \quad (24)$$

where M and K are the mass and stiffness matrices of the Finite Element model, C_d is the damping matrix of the system [39]. The nonlinear VdW interaction force $p(x)$ affects the steady state solution of the linearized system in 2 manners: (i) it both changes the static deflection of the beam u_{ss} , and (ii) acts as an elastic bedding, which changes the natural frequencies of the system. However, the $p(x)$ itself is a function of u_{ss} (see Eq. (13)). Therefore, in order to accurately approximate the linearized elastic bedding, u_{ss} must be first approximated.

3.3 Static deflection approximation

The static equation can be derived from Eq. (24) by nullifying derivatives in time:

$$Kq = \mathbf{Q}\mathbf{p}(x, u_{ss}). \quad (25)$$

The vector \mathbf{p} can be approximated iteratively, using the initial guess of $u_{ss} = 0$. Noticing that the force \mathbf{p} can become singular for $u_{ss}(g_1\zeta_p) = g_2(\zeta_p)$ (see Eq. (13)) it can be deduced that generally, 2 stable steady state solutions are possible, where the singular one is the pull-in solution of the system. Therefore, it is of interest to slowly change the iterative guess of u_{ss} to find the non pull-in solution. This results in the following iterative approximation:

$$u_{ss,n+1} = u_{ss,n} (1 - \varepsilon) + \varepsilon K^{-1} \mathbf{Q}\mathbf{p}(x, u_{ss,n}), \quad \varepsilon < 1 \quad (26)$$

and approximation convergence to of u_{ss} results in

$$\varepsilon K u_{ss,n} = \varepsilon \mathbf{Q} \mathbf{p}(x, u_{ss,n}). \quad (27)$$

which indicates that $u_{ss,n}$ is a solution of the equation. Using the approximated u_{ss} , it is possible to accurately evaluate \mathbf{p} using Eq. (12).

3.4 Linearized model derivation

Having approximated u_{ss} , the linear system can be derived by taking the second derivative of the potential, resulting in:

$$k(x) = \frac{\partial^2 V}{\partial u^2} \bigg|_{\text{equilibrium}} = \int_0^{L_{\text{top}}} \left(\frac{C}{(n-3)} \frac{(g_1(\zeta) - x)^2 - (n-1)(g_2(\zeta) - u_{ss})^2}{\left(\sqrt{(g_1(\zeta) - x)^2 + (g_2(\zeta) - u_{ss})^2} \right)^{n+2}} \right) d\zeta. \quad (28)$$

The resulting linear dynamics of the system will be:

$$M\ddot{q} + C\dot{q} + (K + K_{vdW})q = 0. \quad (29)$$

where K_{vdW} is the projection of the stiffness function presented in Eq. (28) on the state vector q , using the same matrix \mathbf{Q} as before, since $k(x)$ acts as a force.

By solving the generalized eigenvalue problem of the matrices $(M, K + K_{vdW})$ the perturbed natural frequencies are obtained. Therefore, by measuring the natural frequencies of the system, information regarding K_{vdW} can be obtained, and subsequently the topography $(g_1(\zeta), g_2(\zeta))$ can be approximated. However, the dependency between the natural frequencies and the topography is highly coupled and nonlinear. Using a standard gradient descent or Newton procedure to find $g(\zeta)$ is time consuming and leads to convergence and singularity problems (see Appendix B). The latter is because $g(\zeta)$ requires many parameters to accurately describe the topography. This necessitates the implementation of MBSA.

3.5 Successive topography approximation

To apply MBSA, the invertible model $\mathbf{f}_s(g(\zeta))$, is derived. This is done by assuming that firstly, $(g_1(\zeta), g_2(\zeta))$ can be partitioned into sections which are presented either as $(g(\zeta), \zeta)$, where the tip moves perpendicular to the topography, or as $(\zeta, g(\zeta))$, where the tip moves parallel to the topography. Secondly, it is assumed that $g(\zeta)$ can be approximated as a piecewise constant function, and lastly the static forces are neglected, resulting in $u_{ss} \approx 0$. As a result, Eq. (28) becomes:

$$\begin{aligned}
k_{perpendicular}(x) &= \int_0^{L_{top}} \left(\frac{C}{(n-3)} \frac{(\tilde{g}(\zeta) - x)^2 - (n-1)\zeta^2}{\left(\sqrt{(\tilde{g}(\zeta) - x)^2 + \zeta^2}\right)^{n+2}} \right) d\zeta = \\
&\sum_{i=0}^{N-1} \int_{\frac{i}{N}L_{top}}^{\frac{i+1}{N}L_{top}} \left(\frac{C}{(n-3)} \frac{(g_i - x)^2 - (n-1)\zeta^2}{\left(\sqrt{(g_i - x)^2 + \zeta^2}\right)^{n+2}} \right) d\zeta
\end{aligned} \tag{30}$$

for the perpendicular sections, and

$$\begin{aligned}
k_{parallel}(x) &= \int_0^{L_{top}} \left(\frac{C}{(n-3)} \frac{(\zeta - x)^2 - (n-1)g_2(\zeta)^2}{\left(\sqrt{(\zeta - x)^2 + g_2(\zeta)^2}\right)^{n+2}} \right) d\zeta = \\
&\sum_{i=0}^{N-1} \int_{\frac{i}{N}L_{top}}^{\frac{i+1}{N}L_{top}} \left(\frac{C}{(n-3)} \frac{(\zeta - x)^2 - (n-1)g_i^2}{\left(\sqrt{(\zeta - x)^2 + g_i^2}\right)^{n+2}} \right) d\zeta
\end{aligned} \tag{31}$$

To further simplify the model, it is assumed that $k(x)$, being relatively small compared to the bending stiffness, does not change the mode shapes significantly. Therefore, the displacement of a single mode can be approximated as:

$$u = a\phi(x) \tag{32}$$

Substituting Eq. (32) in the modal equation results in:

$$\ddot{a}\phi + \omega_n^2 a\phi + \frac{k(x)}{\rho A} a\phi = 0 \tag{33}$$

By multiplying by ϕ and integrating over the length of the beam, the following equation is obtained:

$$\ddot{a} + \left(\omega_n^2 + \frac{\int_0^{L_{beam}} \phi^2 k(x) dx}{\rho A \int_0^{L_{beam}} \phi^2 dx} \right) a = 0 \tag{34}$$

As a result, the change in the natural frequency can be identified as:

$$\Delta\omega_n^2 = \frac{\int_0^{L_{beam}} \phi^2(x) k(x) dx}{\rho A \int_0^{L_{beam}} \phi^2(x) dx} \tag{35}$$

The latter is the Rayleigh quotient of the added stiffness due to the distributed interactions [38]. In addition to the fact that the mode shapes do not change significantly, their effect on the natural frequency exhibits low sensitivity to perturbations of the mode shape [40]. Furthermore, as was mentioned before, the invertible model does not need to be exact to achieve full convergence. However, this equation is a coupled nonlinear equation, since $\Delta\omega_{n,j}^2$ is a function of all of the parameters of the topography g_i to a negative power. To further simplify the model, it is assumed that the strongest interaction between the topography and the beam is at $\zeta = 0$, where the denominator of the function under the integral is smallest. Therefore, other interactions are neglected, resulting in the invertible model:

$$\Delta\omega_{n,i}'^2 = \frac{L_{top}}{N} \frac{C}{(n-3)} \frac{\int_0^{L_{beam}} \frac{\phi^2(x)}{(g_i - x)^n} dx}{\int_0^{L_{beam}} \phi^2(x) dx} \quad (36)$$

for the perpendicular sections of the topography, and

$$\Delta\omega_{n,i}'^2 = \frac{L_{top}}{N} \frac{C}{(n-3)} \frac{\int_0^{L_{beam}} \frac{x^2 - (n-1)g_i^2}{\left(\sqrt{x^2 + g_i^2}\right)^{n+2}} \phi^2(x) dx}{\int_0^{L_{beam}} \phi^2(x) dx} \quad (37)$$

for the parallel sections.

Note that the invertible system is a set of decoupled nonlinear equations of the single parameter g_i which can be easily obtained. By measuring the change in the natural frequency corresponding to each piecewise constant segment g_i in the topography, the set of equations (36) and (37) can be solved, resulting in an approximation of the topography \mathbf{g}' . The measured perturbation in the natural frequency is used for the iterative approximation method, where \mathbf{g}' converges to the real topography \mathbf{g} . It is important to note that AR was used to measure the natural frequency of the beam. AR allows the automatic locking onto the system's resonance frequency [32,34,41]. By taking the response of the system, phase shifting it in 90 degrees and putting it through a relay, the system is automatically excited in resonance

4. Simulation results

A simulation of a gold nanofiber interacting with a silicon made topography, was conducted. the constants and parameters of the simulation and their derivation are detailed in Appendix C. The approximation of

the topography was executed in the following steps: first, the natural frequency of the fiber, when vibrating perpendicular to the topography, was measured (see Figure 3.A, and Video 1). Next, the measurement of the natural frequency at each point is used to approximate the perpendicular part of the topography and indicate the existence of a groove, as presented in Figure 3.B (see Video 2), using MBSA. Then, the lower sidewall was measured via the change in the natural frequency of the fiber (see Figure 4.A and Video 3), and the sidewall was also approximated (see Figure 4.B and Video 4). In the same manner, the upper sidewall and the base were approximated, resulting in the full approximation of the topography (Figure 5).

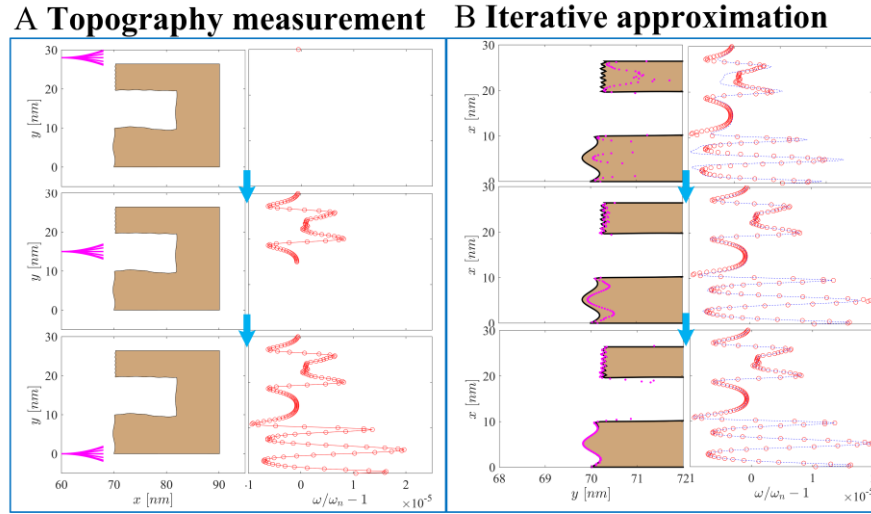
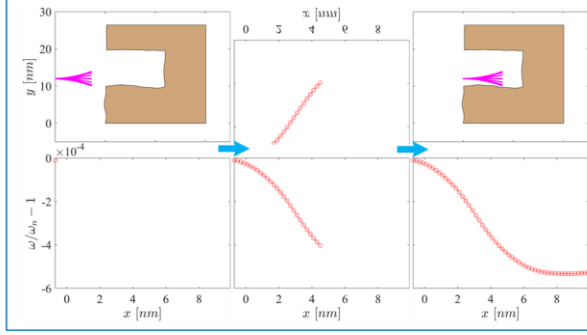


Figure 3 - The approximation method. Section A shows the measurement of the natural frequency (in red) of the fiber (in magenta) when positioned perpendicular to different points in the topography (in brown). Section B shows the iterative convergence of the topography approximation (in magenta) to the exact topography (in brown) simultaneously with the convergence of the approximated frequency vector (in blue) to the measured one (in red).

A Sidewall measurement



B Sidewall approximation

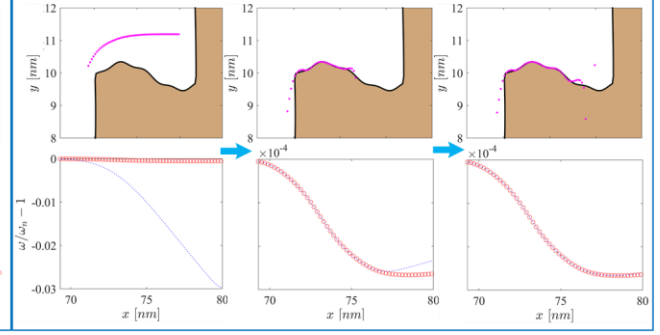


Figure 4 – The sidewall approximation. Section A shows the measurement of the natural frequency (in red) of the fiber (in magenta) when positioned parallel to different points in the lower sidewall of the topography (in brown). Section B shows the convergence of the approximation of the sidewall to the exact topography.

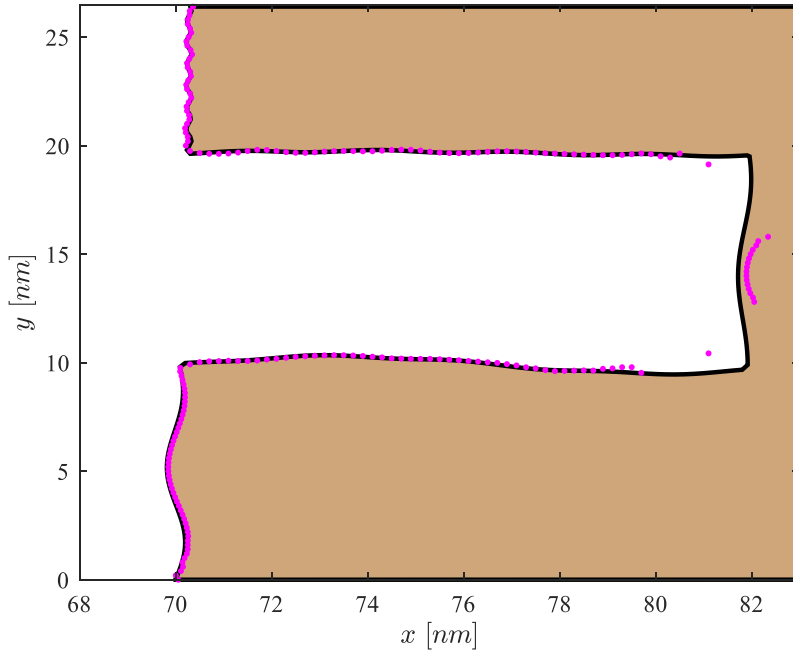


Figure 5 - the full topography approximation.

5. Experimental results

The proposed method was verified using a magnetic system (see Figure 6) which substitutes the VdW potential with a magnetic one since they have similar characteristics in certain configurations (see Appendix D). The potential constants C and n of the system were calibrated using a known magnetic topography (see Appendix E).

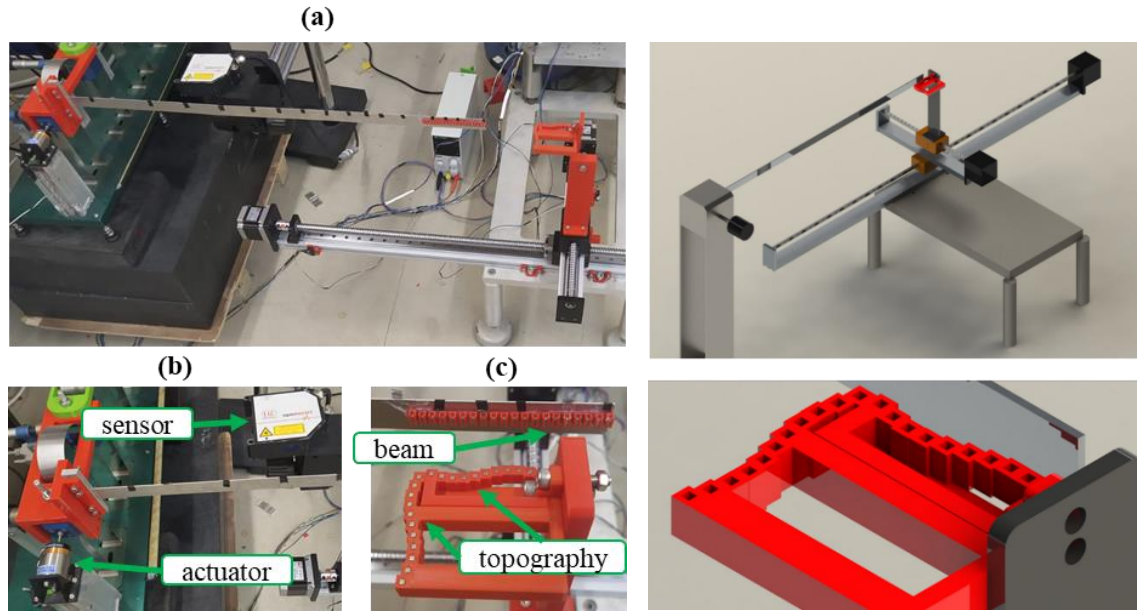


Figure 6 - The magnetic experimental system. (a) The full system. (b) The sensor measuring the beam vibration and the actuator applying the sinusoidal excitation. (c) The measured topography and the magnetic beam. The potential constants were curve-fitted, and the topography was approximated via the calibrated potential

The actuated beam is a 0.682 meters long aluminum beam, with a rectangular cross-section of 21 by 1 mm. The approximation set was measured by moving the beam across the topography at a nominal distance of 20 [mm] and measuring the natural frequency (see Video 5). Using the measurements, the perpendicular topography was approximated using MBSA methodology (see Figure 7 and Video 6), and the beam was inserted parallel to the topography, to approximate the groove sidewall (see Figure 8 and Video 6). The full topography is constructed from the two approximated parts, as presented in Figure 9:

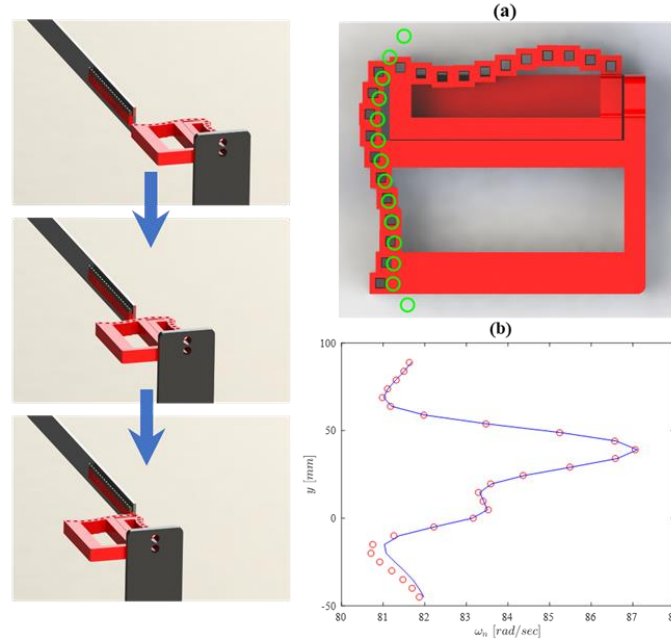


Figure 7 - The topography approximation process. The left side depicts the measurement process of the perpendicular part of the topography. (a) shows the approximation results, and (b) shows the approximated and measured frequency vector

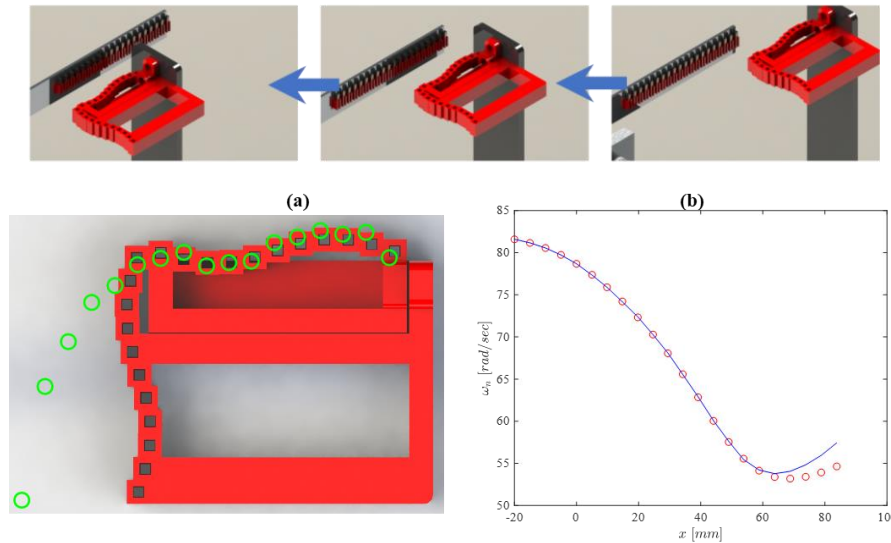


Figure 8 - The topography approximation process. The upper panels depict the measurement process of the parallel part of the topography. (a) shows the approximation results, and (b) shows the approximated and measured frequency vector

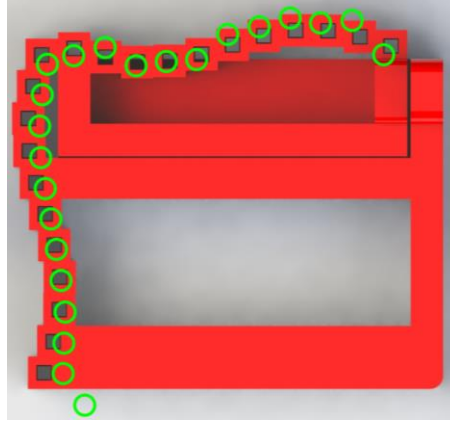


Figure 9 - The full topography approximation, using MBSA.

The error percentages of the approximation are presented in Figure 10:

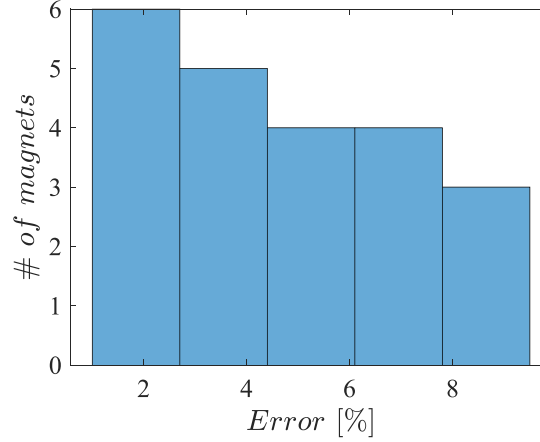


Figure 10 – A histogram of the errors for each magnet.

It is evident that MBSA approximates the measured topography with reasonable accuracy, overcoming the coupled interactions. Residual magnetic fields and geometrical errors may cause some deviations from the true magnets and their estimated locations. Additionally, the variance in the magnetic potential of the individual magnets adds to the inaccuracy. It is expected that nanoscale, the atomic or molecular interactions can be better described with the proposed approach, leading to a more accurate approximation.

6. Discussion and conclusions

A method for inverting a set of nonlinear equations and thus accurately approximating a set of parameters was proposed. The criterion that guarantees the convergence of the method was presented and the

procedure was validated both on a simulated case study of a thin nanofiber interacting with a groove and an up-scaled system that substitutes VdW interaction forces with magnetic ones. Experimental results validate the ability to accurately invert complex multivariable nonlinear systems, using a simplified model.

Appendix A – An iterative approximation method for the solution of a set of nonlinear equations

It is of interest to solve the set of nonlinear equations, which can be represented as:

$$\mathbf{f}(\mathbf{g}, \mathbf{x}) = \boldsymbol{\omega}_d^2, \quad \boldsymbol{\omega}_d^2 \in \mathbb{R}^N, \quad \mathbf{g} \in \mathbb{R}^M \quad (38)$$

Where \mathbf{f} represents the system model, which in the context of this paper is represented in Eq.(13), \mathbf{g} is the unknown piecewise constant parametric topography vector we wish to approximate, and $\boldsymbol{\omega}_d^2$ is the measurement vector used to approximate \mathbf{g} . It is assumed that \mathbf{f} is an injective function so that every value of $\boldsymbol{\omega}_d^2$ corresponds to a single \mathbf{g} .

While \mathbf{f} is not easily invertible, there is a different equation:

$$\mathbf{f}_s(\mathbf{g}, \mathbf{x}) = \boldsymbol{\omega}'^2 \quad (39)$$

which is solvable for \mathbf{g} . However, the vector $\boldsymbol{\omega}'^2$ is unknown. Therefore, it is of interest to find the vector $\boldsymbol{\omega}'^2$ for which Eq. (39) will result in the correct \mathbf{g} . Having found $\boldsymbol{\omega}'^2$, \mathbf{f}_s can be inverted in a straight forward and numerically robust manner to find an approximation of \mathbf{g} .

This will be done using 4 iterative steps:

Step 1: Solve Eq. (39) for $\mathbf{g} = \mathbf{g}'_k$ using the estimate of $\boldsymbol{\omega}'^2$ at the k^{th} iteration, denoted, $\boldsymbol{\omega}'^2_k$, i.e:

$$\mathbf{g}'_k = \mathbf{f}_s^{-1}(\boldsymbol{\omega}'^2_k) \quad (40)$$

Step 2: Calculate the deviation in $\boldsymbol{\omega}$ from the true value $\boldsymbol{\omega}_d^2$ (note that $\mathbf{f}(\mathbf{g}'_k, \mathbf{x})$ is exact and can be evaluated directly:

$$\mathbf{e}_k = \boldsymbol{\omega}_d^2 - \mathbf{f}(\mathbf{g}'_k, \mathbf{x}) \quad (41)$$

Step 3: Update the input function to Eq. (40):

$$\boldsymbol{\omega}'^2_{k+1} = \boldsymbol{\omega}'^2_k + \Delta \boldsymbol{\omega}'^2 \quad (42)$$

It should be stated that $\Delta \boldsymbol{\omega}'^2$ is some a function of the error, which will be chosen so that the norm of the error decreases.

Step 4: Repeat. Steps 1-3 using $\boldsymbol{\omega}'^2_{k+1}$.

A.1 Conditions for convergence.

Taking the k^{th} iteration, where the first iteration is:

$$\boldsymbol{\omega}'^2_1 \triangleq \boldsymbol{\omega}_d^2 \quad (43)$$

Eq. (39) can be solved, resulting in:

$$\mathbf{g}'_k = \mathbf{f}_s^{-1}(\boldsymbol{\omega}'^2_k) \quad (44)$$

The calculated \mathbf{g}'_k can be substituted into Eq.(38), resulting in the error of the full equation (Eq. (38)):

$$\mathbf{e}_k = \boldsymbol{\omega}_d^2 - \mathbf{f}(\mathbf{g}'_k) \quad (45)$$

The error of the solvable equation (Eq. (39)) is:

$$\mathbf{e}_{s,k} = \boldsymbol{\omega}'^2 - \boldsymbol{\omega}'^2_k \quad (46)$$

The system will converge if

$$\|\mathbf{e}_{s,k+1}\| < \|\mathbf{e}_{s,k}\| \quad (47)$$

Substituting Eq. (46) into (47):

$$\|\mathbf{e}_{s,k+1}\|^2 = (\boldsymbol{\omega}'^2 - \boldsymbol{\omega}'^2_k - \Delta\boldsymbol{\omega}'^2)^T (\boldsymbol{\omega}'^2 - \boldsymbol{\omega}'^2_k - \Delta\boldsymbol{\omega}'^2) = \|\mathbf{e}_{s,k}\|^2 + \|\Delta\boldsymbol{\omega}'^2\|^2 - 2\mathbf{e}_{s,k}^T \Delta\boldsymbol{\omega}'^2 \quad (48)$$

For Eq. (47) to hold, the following must be dictated:

$$\|\Delta\boldsymbol{\omega}'^2\|^2 < 2\mathbf{e}_{s,k}^T \Delta\boldsymbol{\omega}'^2 \quad (49)$$

By choosing:

$$\Delta\boldsymbol{\omega}'^2 = \beta \mathbf{e}_k, \beta > 0 \quad (50)$$

And substituting into Eq. (49):

$$\beta \|\mathbf{e}_k\|^2 < 2\mathbf{e}_{s,k}^T \mathbf{e}_k \quad (51)$$

Since β can be chosen to be arbitrarily small, it is enough to show that

$$0 < 2\mathbf{e}_{s,k}^T \mathbf{e}_k. \quad (52)$$

This choice of $\Delta\boldsymbol{\omega}'^2$ allows us to rearrange Eq. (42) as:

$$\boldsymbol{\omega}'^2_{k+1} = \boldsymbol{\omega}'^2_k + \beta \left(\boldsymbol{\omega}_d^2 - \mathbf{f}(\mathbf{f}_s^{-1}(\boldsymbol{\omega}'^2_k)) \right) \quad (53)$$

Using the fundamental theorem of calculus:

$$\begin{aligned}\mathbf{e}_k &= \mathbf{f}(\mathbf{g}) - \mathbf{f}(\mathbf{g}'_k) = (\mathbf{g} - \mathbf{g}'_k) \int_0^1 \frac{\partial \mathbf{f}}{\partial \mathbf{g}}(\mathbf{g} + \lambda(\mathbf{g} - \mathbf{g}'_k)) d\lambda, \lambda \in [\mathbf{g}'_k, \mathbf{g}] \\ \mathbf{e}_{s,k} &= \mathbf{f}_s(\mathbf{g}) - \mathbf{f}_s(\mathbf{g}'_k) = (\mathbf{g} - \mathbf{g}'_k) \int_0^1 \frac{\partial \mathbf{f}_s}{\partial \mathbf{g}}(\mathbf{g} + \lambda(\mathbf{g} - \mathbf{g}'_k)) d\lambda, \lambda \in [\mathbf{g}'_k, \mathbf{g}]\end{aligned}\quad (54)$$

Eq. (52) is therefore:

$$(\mathbf{g} - \mathbf{g}'_k)^T \int_0^1 \left[\frac{\partial \mathbf{f}_s}{\partial \mathbf{g}^T}(\mathbf{g} + \lambda(\mathbf{g} - \mathbf{g}'_k)) \right] d\lambda \int_0^1 \left[\frac{\partial \mathbf{f}}{\partial \mathbf{g}^T}(\mathbf{g} + \lambda(\mathbf{g} - \mathbf{g}'_k)) \right] d\lambda (\mathbf{g} - \mathbf{g}'_k) > 0 \quad (55)$$

using Taylor expansion, assuming $\mathbf{g} - \mathbf{g}_k$ is relatively small:

$$\begin{aligned}\mathbf{e}_k &= \mathbf{f}(\mathbf{g}) - \mathbf{f}(\mathbf{g}'_k) \approx \frac{\partial \mathbf{f}}{\partial \mathbf{g}}(\mathbf{g} - \mathbf{g}'_k) \\ \mathbf{e}_{s,k} &= \mathbf{f}_s(\mathbf{g}) - \mathbf{f}_s(\mathbf{g}'_k) \approx \frac{\partial \mathbf{f}_s}{\partial \mathbf{g}}(\mathbf{g} - \mathbf{g}'_k)\end{aligned}\quad (56)$$

Eq. (52) can be approximated as:

$$(\mathbf{g} - \mathbf{g}'_k)^T \left(\frac{\partial \mathbf{f}_s}{\partial \mathbf{g}} \right)^T \frac{\partial \mathbf{f}}{\partial \mathbf{g}} (\mathbf{g} - \mathbf{g}'_k) > 0 \quad (57)$$

Therefore, Eq. (57) holds iff the matrix $\left(\frac{\partial \mathbf{f}_s}{\partial \mathbf{g}^T} \right)^T \frac{\partial \mathbf{f}}{\partial \mathbf{g}^T}$ is positive definite. In addition, when the system converges:

$$\boldsymbol{\omega}'_{k+1} = \boldsymbol{\omega}'_k \rightarrow \Delta \boldsymbol{\omega}'^2 = 0. \quad (58)$$

This happens only when $\mathbf{e}_i = 0$, which results in

$$\mathbf{g}'_k = \mathbf{g} \quad (59)$$

since the system is injective.

Therefore, if Eq. (52) holds, the method will converge to the desired \mathbf{g} .

Appendix B – An illustrative example of the implementation of MBSA

Consider the single parameter function:

$$f(x) = \sin(15x) + 8x + 3 \quad (60)$$

It is of interest to approximate the solution of the problem:

$$f(x)=0 \quad (61)$$

By implementing gradient descent, with the naïve initial guess of $x_0 = 0$, the optimization method converges to a local minimum. i.e (0.1409,1.1065) (see Figure 11.a). This is a sub-optimal result. However, by implementing a simplified invertible model:

$$f_s(x)=6x=\omega, \quad \omega_0 = 0 \quad (62)$$

For which the inverse is:

$$f_s^{-1}(\omega) = \frac{\omega}{6} = x_s \quad (63)$$

it is possible to implement MBSA. Notice that the inverse model is inexact, neglecting the sinusoidal component and DC component and inaccurately approximating the gradient of the linear component. However, it still maintains the general gradient of the function.

Following Eq. (53), the iterative law will be:

$$\omega_{k+1} = \omega_k + \beta \left(\omega_n - f \left(\frac{\omega_k}{6} \right) \right) = \omega_k + \beta \left(\omega_n - \left(\sin \left(\frac{15\omega_k}{6} \right) + \frac{8\omega_k}{6} + 3 \right) \right) \quad (64)$$

This method results in the convergence to the desired solution, as presented in Figure 11.b

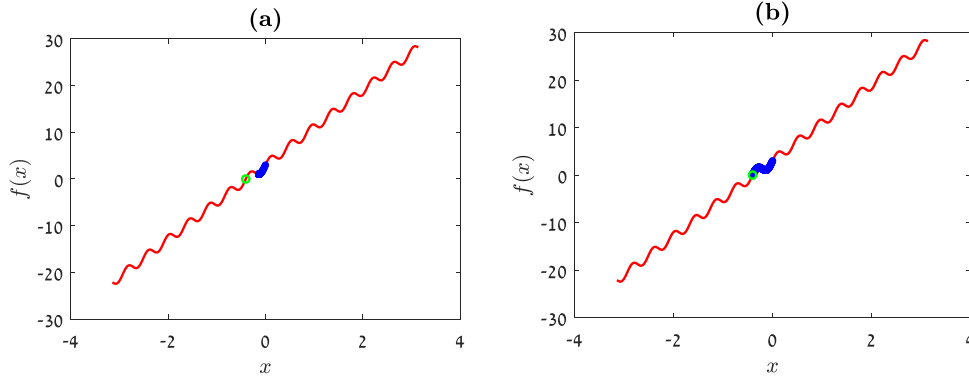


Figure 11 - Convergence of the different optimization methods searching for a result to the equation $\sin(5x) + 8x + 3 = 0$. The optimized function is in red, the optimization steps are in blue, and the optimal point (0) is in green. (a): Gradient based optimization. (b): MBSA optimization

To prove the convergence of MBSA in this problem, it will be shown that Eq. (52) holds. Substituting Eq. (45) and (46) into Eq. (52):

$$\mathbf{e}^T \mathbf{e}_s = \left(8(x - x_d) + 2 \cos \left(\frac{15}{2}(x + x_d) \right) \sin \left(\frac{15}{2}(x - x_d) \right) \right) 6(x - x_d) \quad (65)$$

For $|x - x_d| > 1/4$ we get

$$2\beta \mathbf{e}^T \mathbf{e}_s > \varepsilon (x - x_d)^2, \quad \varepsilon > 0. \quad (66)$$

Which results in the system converging. However, for

$$\left(8(x - x_d) + 2\cos\left(\frac{15}{2}(x + x_d)\right)\sin\left(\frac{15}{2}(x - x_d)\right) \right) 6(x - x_d) < 0 \quad (67)$$

And $|x - x_d| < 1/4$, the system diverges. Now, applying Taylor expansion in the form of:

$$\sin\left(\frac{15}{2}(x - x_d)\right) \approx \frac{15}{2}(x - x_d) \triangleq \frac{15}{2}\Delta x \quad (68)$$

Results in

$$(8 + 15\cos(15(x_d + \Delta x)))6\Delta x^2 < 0. \quad (69)$$

Note that the function in brackets is $f'(x)$, which results in the state: $f(x_d) = 0$, $f'(x_d) < 0$. However, since it is known that there exists some x for which $f(x) > 0$, there must be another crossing of $f(x_{d,2}) = 0$, $f'(x_{d,2}) > 0$, for which Eq. (52) does hold, resulting in the convergence to $x_{d,2}$. As a result, the system converges to the point $f(x_d) = 0$ for any initial condition.

It is worth noting that this result holds regardless of the amplitudes of the sinusoidal and linear components. In addition, while MBSA was demonstrated on a single parameter system, this method can be extended to multiple parameters, provided an invertible model with similar gradients is constructed.

Appendix C - Method simulation constants

For the simulation, the interaction forces between a gold nanowire and a silicon topography were implemented using the Lennard – Jones approximation of the Van der Waals Potential [35,36]:

$$V = -4\varepsilon \left(\frac{\sigma}{r} \right)^6 \left[kJmol^{-1} \right] \quad (70)$$

The values of the parameters ε and σ for gold and silicon are [42]:

Constants	Gold	Silicon
$\sigma [nm]$	0.293373	0.392
$\varepsilon \left[\frac{kJ}{mol} \right]$	0.163176	2.51040

The constants σ_{s-g} , ε_{s-g} which are used to construct the potential acting between silicon and gold, can be approximated as [43]:

$$\sigma_{s-g} = \frac{1}{2}(\sigma_s + \sigma_g) \quad (71)$$

$$\varepsilon_{s-g} = \sqrt{\varepsilon_s \varepsilon_g} . \quad (72)$$

Appendix D - Magnetic potential

Magnetic forces have similar properties to Van der Waals interaction forces since in the proper configuration they are also a function of the distance by a certain power.

The interaction potential between two dipoles can be approximated as [44]:

$$V = -\frac{C}{r^3} (3(I_1 \cdot \hat{r})(I_2 \cdot \hat{r}) - (I_1 \cdot I_2)) \quad (73)$$

where C is a constant resulting from the magnetic moments and permeability, r is the distance between the two centers of the moments, \hat{r} is the normalized vector in the direction of r , and I_1, I_2 are the normalized vectors in the directions of the first and second dipoles respectively. Assuming the vectors I_1, I_2 are parallel with opposite signs, and that \hat{r} is orthogonal to I_1, I_2 , the force becomes:

$$V = -\frac{C}{r^3} . \quad (74)$$

These forces can be somewhat analogous to Van der Waals forces, and therefore this configuration can be used to validate the method of identification.

Appendix E - Magnetic potential calibration

To find the potential constants C and n , the system was calibrated using a single magnet. The natural frequency was measured at different known distances from the beam. Eq. (28) was used to approximate and the values of C , n and ω_0 using nonlinear least squares, with \mathbf{g} being a known topography. The calibration set and its approximation are presented in Figure 12:

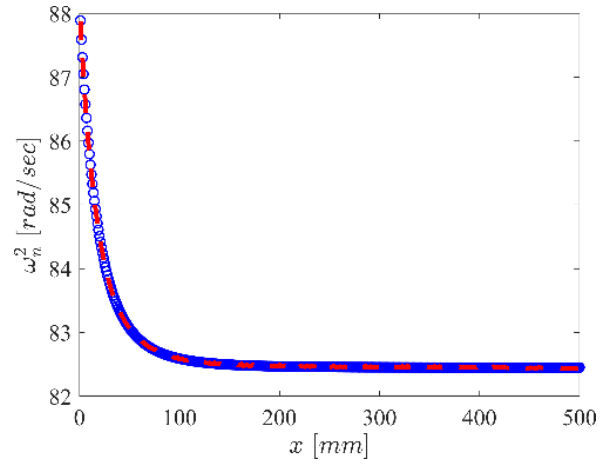


Figure 12– The calibration set. In red is the measured set. In blue is the approximated set using the calibrated parameters.

The error between the measured and approximated natural frequency is small, indicating a precise approximation of C and n .

Acknowledgments

The Authors would like to thank the valuable comments of Professor Keegan Moore and the preparatory work done by Mr. Nir Ben Shaya in his MSc research, supporting some of the initial work presented here.

References

- [1] K.J. Åström, P. Eykhoff, System identification-A survey, *Automatica*. 7 (1971) 123–162. [https://doi.org/10.1016/0005-1098\(71\)90059-8](https://doi.org/10.1016/0005-1098(71)90059-8).
- [2] P. Goodwin, G. C., GC, G., & RL, DYNAMIC SYSTEM IDENTIFICATION. EXPERIMENT DESIGN AND DATA ANALYSIS, 1977.
- [3] GOODWIN GC, Optimal input signals for nonlinear- system identification, *Proc. Inst. Electr. Eng.* 118 (1971). <https://doi.org/10.1049/piee.1971.0183>.
- [4] C.R. Rojas, J.S. Welsh, G.C. Goodwin, A. Feuer, Robust optimal experiment design for system identification, *Automatica*. 43 (2007). <https://doi.org/10.1016/j.automatica.2006.12.013>.
- [5] G.C. Goodwin, J.C. Murdoch, R.L. Payne, Optimal test signal design for linear S.I.S.O. system identification, *Int. J. Control*. 17 (1973). <https://doi.org/10.1080/00207177308932357>.
- [6] G.C. Goodwin, M.B. Zarrop, R.L. Payne, Coupled Design of Test Signals, Sampling Intervals, and Filters for System Identification, *IEEE Trans. Automat. Contr.* 19 (1974). <https://doi.org/10.1109/TAC.1974.1100715>.
- [7] Z.H. Qureshi, T.S. Ng, G.C. Goodwinj, Optimum experimental design for identification of distributed parameter systems, *Int. J. Control*. 31 (1980). <https://doi.org/10.1080/00207178008961025>.
- [8] G. Kerschen, K. Worden, A.F. Vakakis, J.C. Golinval, Past, present and future of nonlinear system identification in structural dynamics, *Mech. Syst. Signal Process.* 20 (2006). <https://doi.org/10.1016/j.ymssp.2005.04.008>.
- [9] J. Bongard, H. Lipson, Automated reverse engineering of nonlinear dynamical systems, *Proc. Natl. Acad. Sci. U. S. A.* 104 (2007). <https://doi.org/10.1073/pnas.0609476104>.
- [10] M. Schmidt, H. Lipson, Distilling free-form natural laws from experimental data, *Science* (80-.). 324 (2009). <https://doi.org/10.1126/science.1165893>.
- [11] H. Schaeffer, R. Caflisch, C.D. Hauck, S. Osher, Sparse dynamics for partial differential equations, *Proc. Natl. Acad. Sci. U. S. A.* 110 (2013). <https://doi.org/10.1073/pnas.1302752110>.
- [12] V. Ozoliņš, R. Lai, R. Caflisch, S. Osher, Compressed modes for variational problems in

- mathematics and physics, *Proc. Natl. Acad. Sci. U. S. A.* 110 (2013). <https://doi.org/10.1073/pnas.1318679110>.
- [13] S.L. Brunton, J.L. Proctor, J.N. Kutz, W. Bialek, Discovering governing equations from data by sparse identification of nonlinear dynamical systems, *Proc. Natl. Acad. Sci. U. S. A.* 113 (2016). <https://doi.org/10.1073/pnas.1517384113>.
- [14] S.M. Udrescu, M. Tegmark, AI Feynman: A physics-inspired method for symbolic regression, *Sci. Adv.* 6 (2020). <https://doi.org/10.1126/sciadv.aay2631>.
- [15] M. Raissi, P. Perdikaris, G.E. Karniadakis, Physics-informed neural networks: A deep learning framework for solving forward and inverse problems involving nonlinear partial differential equations, *J. Comput. Phys.* (2019). <https://doi.org/10.1016/j.jcp.2018.10.045>.
- [16] A. Rasheed, O. San, T. Kvamsdal, Digital twin: Values, challenges and enablers from a modeling perspective, *IEEE Access.* 8 (2020). <https://doi.org/10.1109/ACCESS.2020.2970143>.
- [17] A. Bjork, C.L. Lawson, R.J. Hanson, Solving Least Squares Problems, *Math. Comput.* 30 (1976). <https://doi.org/10.2307/2005340>.
- [18] G.A.G. Cidade, C. Anteneodo, N.C. Roberty, A.J. Silva Neto, A generalized approach for atomic force microscopy image restoration with Bregman distances as Tikhonov regularization terms, *Inverse Probl. Eng.* 8 (2000). <https://doi.org/10.1080/174159700088027741>.
- [19] T. Ando, T. Uchihashi, T. Fukuma, High-speed atomic force microscopy for nano-visualization of dynamic biomolecular processes, *Prog. Surf. Sci.* 83 (2008) 337–437. <https://doi.org/10.1016/J.PROGSURF.2008.09.001>.
- [20] Y. Martin, H.K. Wickramasinghe, Method for imaging sidewalls by atomic force microscopy, *Appl. Phys. Lett.* (1994). <https://doi.org/10.1063/1.111578>.
- [21] D. Hussain, K. Ahmad, J. Song, H. Xie, Advances in the atomic force microscopy for critical dimension metrology, *Meas. Sci. Technol.* (2017). <https://doi.org/10.1088/0957-0233/28/1/012001>.
- [22] J. Choi, B.C. Park, S.J. Ahn, D.-H. Kim, J. Lyou, R.G. Dixon, N.G. Orji, J. Fu, T. V. Vorburger, Evaluation of carbon nanotube probes in critical dimension atomic force microscopes, *J. Micro/Nanolithography, MEMS, MOEMS.* (2016). <https://doi.org/10.1117/1.jmm.15.3.034005>.
- [23] V. Mancevski, P.F. McClure, Development of a dual-probe Caliper CD-AFM for near model-independent nanometrology, in: *Metrol. Insp. Process Control Microlithogr. XVI*, 2002. <https://doi.org/10.1117/12.473418>.
- [24] L. Nony, A. Baratoff, D. Schär, O. Pfeiffer, A. Wetzel, E. Meyer, Noncontact atomic force microscopy simulator with phase-locked-loop controlled frequency detection and excitation, *Phys. Rev. B - Condens. Matter Mater. Phys.* 74 (2006). <https://doi.org/10.1103/PhysRevB.74.235439>.

- [25] G. Binnig, C.F. Quate', E.L. Gi, C. Gerber, Atomic Force Microscope, n.d.
- [26] S. Santos, V. Barcons, H.K. Christenson, J. Font, N.H. Thomson, The intrinsic resolution limit in the atomic force microscope: Implications for heights of nano-scale features, PLoS One. (2011). <https://doi.org/10.1371/journal.pone.0023821>.
- [27] THE METHOD OF SUCCESSIVE APPROXIMATIONS FOR FUNCTIONAL EQUATIONS, n.d.
- [28] S. Mortezaipoor, E.K.F. Lee, A 1-V, 8-Bit Successive Approximation ADC in Standard CMOS Process, IEEE J. Solid-State Circuits. 35 (2000) 642–646. <https://doi.org/10.1109/4.839925>.
- [29] X. Li, Demosaicing by successive approximation, IEEE Trans. Image Process. 14 (2005) 370–379. <https://doi.org/10.1109/TIP.2004.840683>.
- [30] G.Y. Tang, Suboptimal control for nonlinear systems: a successive approximation approach, Syst. Control Lett. 54 (2005) 429–434. <https://doi.org/10.1016/J.SYSCONLE.2004.09.012>.
- [31] J.E. Sader, S.P. Jarvis, Accurate formulas for interaction force and energy in frequency modulation force spectroscopy, Appl. Phys. Lett. 84 (2004). <https://doi.org/10.1063/1.1667267>.
- [32] E. Rubin, S. Davis, I. Bucher, Multidimensional topography sensing simulating an AFM, Sensors Actuators, A Phys. 303 (2020). <https://doi.org/10.1016/j.sna.2019.111690>.
- [33] V.I. Babitsky, Autoresonant mechatronic systems, Mechatronics. (1995). [https://doi.org/10.1016/0957-4158\(95\)00026-2](https://doi.org/10.1016/0957-4158(95)00026-2).
- [34] K.J. Aström, G.C. Goodwin, P.R. Kumar, Adaptive control, filtering, and signal processing, 2012.
- [35] J.E. Lennard-Jones, Cohesion, Proc. Phys. Soc. (1931). <https://doi.org/10.1088/0959-5309/43/5/301>.
- [36] C. Argento, A. Jagota, W.C. Carter, Surface formulation for molecular interactions of macroscopic bodies, J. Mech. Phys. Solids. 45 (1997) 1161–1183. [https://doi.org/10.1016/S0022-5096\(96\)00121-4](https://doi.org/10.1016/S0022-5096(96)00121-4).
- [37] S. Timoshenko, History of strength of materials, Courier Corporation, 1983.
- [38] K.J. Bathe, Finite Element Procedures, 1996.
- [39] M. Géradin, D. Rixen, Mechanical Vibrations: Theory and Application to Structural Dynamics, West Sussex, UK, 2014.
- [40] , L Meirovitch, , RG Parker, Fundamentals of Vibrations, Appl. Mech. Rev. 54 (2001) B100–B101. <https://doi.org/10.1115/1.1421112>.
- [41] S. Davis, I. Bucher, Automatic vibration mode selection and excitation; combining modal filtering with autoresonance, Mech. Syst. Signal Process. 101 (2018) 140–155. <https://doi.org/10.1016/j.ymssp.2017.08.009>.

- [42] G. Munaò, A. Correa, A. Pizzirusso, G. Milano, On the calculation of the potential of mean force between atomistic nanoparticles, *Eur. Phys. J. E.* (2018). <https://doi.org/10.1140/epje/i2018-11646-3>.
- [43] A.K. Rappé, C.J. Casewit, K.S. Colwell, W.A. Goddard, W.M. Skiff, UFF, a Full Periodic Table Force Field for Molecular Mechanics and Molecular Dynamics Simulations, *J. Am. Chem. Soc.* (1992). <https://doi.org/10.1021/ja00051a040>.
- [44] W.S. Price, *Spin dynamics: Basics of nuclear magnetic resonance*, 2nd edition., Concepts Magn. Reson. Part A. (2009). <https://doi.org/10.1002/cmr.a.20130>.

Figure 1 - A flowchart of the suggested successive approximation method 7

Figure 2 - The schematics of the simulated system. The oscillating fiber (in blue) interacts with the topography sample (in orange) resulting in distributed forces (in green) depending on the gap (r) between each point on the fiber and any point on the measured topography, illustrated by the red arrow. On the right, an artist's concept of the sensor and some illustrated topography is depicted. 7

Figure 3 - The approximation method. Section A shows the measurement of the natural frequency (in red) of the fiber (in magenta) when positioned perpendicular to different points in the topography (in brown). Section B shows the iterative convergence of the topography approximation (in magenta) to the exact topography (in brown) simultaneously with the convergence of the approximated frequency vector (in blue) to the measured one (in red). 14

Figure 4 – The sidewall approximation. Section A shows the measurement of the natural frequency (in red) of the fiber (in magenta) when positioned parallel to different points in the lower sidewall of the topography (in brown). Section B shows the convergence of the approximation of the sidewall to the exact topography. 15

Figure 5 - the full topography approximation. 15

Figure 6 - The magnetic experimental system. (a) The full system. (b) The sensor measuring the beam vibration and the actuator applying the sinusoidal excitation. (c) The measured topography and the

magnetic beam. The potential constants were curve-fitted, and the topography was approximated via the calibrated potential 16

Figure 7 - The topography approximation process. The left side depicts the measurement process of the perpendicular part of the topography. (a) shows the approximation results, and (b) shows the approximated and measured frequency vector 17

Figure 8 - The topography approximation process. The upper panels depict the measurement process of the parallel part of the topography. (a) shows the approximation results, and (b) shows the approximated and measured frequency vector 17

Figure 9 - The full topography approximation, using MBSA. 18

Figure 10 – A histogram of the errors for each magnet. 18

Figure 11 - Convergence of the different optimization methods searching for a result to the equation $\sin(5x) + 8x + 3 = 0$. The optimized function is in red, the optimization steps are in blue, and the optimal point (0) is in green. (a): Gradient based optimization. (b): MBSA optimization 23

Figure 12– The calibration set. In red is the measured set. In blue is the approximated set using the calibrated parameters. 26

Video 1 (separate file). Measurement of the change in the natural frequency due to the interaction with the perpendicular part of the topography

Video 2 (separate file). Approximation of the perpendicular topography using MBSA

Video 3 (separate file). Measurement of the change in the natural frequency due to the interaction with the topography sidewall.

Video 4 (separate file). Approximation of the topography sidewall using MBSA

Video 5 (separate file). Measurement of change in the natural frequency due to magnetic topography.

Video 6 (separate file). Approximation of the magnetic topography using MBSA